JMEPEG
https://doi.org/10.1007/s11665-024-10383-z

ORIGINAL RESEARCH ARTICLE

Validation of x-Ray Computed Tomography Detection Limits for Stochastic Flaws in Additively Manufactured Ti-6Al-4 V

Griffin Jones, Veeraraghavan Sundar, Rachel Reed, Marissa Stecko, and Jayme Keist

Submitted: 26 June 2024 / Revised: 20 September 2024 / Accepted: 5 October 2024

X-ray computed tomography (XCT) continues to be a primary means of defining flaw populations in fatigue-critical components fabricated by additive manufacturing (AM), and therefore, defining the detection capability of XCT is necessary. Stochastic flaw populations from four samples from a laser powder bed fusion (L-BPF) build of Ti-6Al-4V fatigue specimens were interrogated with XCT scans at various voxel sizes, followed by automated optical serial sectioning (AOSS) with a Robo-Met.3D system as a higher fidelity technique for comparison. Data sets were registered and processed with an automated defect recognition (ADR) algorithm. Comparison of the detected flaw populations showed a two to three orders of magnitude greater quantity in the AOSS data, with significant improvement in the XCT detection rate with refinement of voxel size. Although refined voxel size XCT scans revealed additional flaws, detection of 90% of the "ground truth" flaws present in the AOSS data was not achieved until flaws reached a size of 7-17 times the voxel size of the XCT scan. The need for additional study of targeted flaw sizes to validate and refine these predictions was identified.

Keywords additive manufacturing, defect detection, fatigue, nondestructive testing, serial sectioning, x-ray computed tomography

1. Introduction

Additive manufacturing (AM) of metallic components has become a widely adopted technology over the past decade (Ref 1-3). The additional design space, potential for novel performance enhancements and supply chain advantages offered by techniques such as laser powder bed fusion (L-PBF) AM have garnered much interest from the aerospace, maritime and defense industries. Adoption of its widespread use for critical applications has been slowed, however, by uncertainty about the flaws created by the process, and the impact of those flaws (Ref 4, 5). Significant work has gone into understanding the foundational process–structure–property relationships created by various metal AM processes (Ref 6). For Ti-6Al-4V, the alloy of interest for this study, the direct effect of processing defects on resultant mechanical properties has been well investigated (Ref 7), with several x-ray-based techniques (Ref 8) including time-lapse observation (Ref 9). Mower and Long found that L-PBF Ti-6Al-4V, tested in the as-deposited state, yielded significantly lower fatigue strength than wrought material, due to the presence of surface, near-surface and internal flaws (Ref 10). Hot isostatic pressing (HIP) was identified as a means of decreasing the variability in fatigue life of Ti-6Al-4V (Ref 11-13), though not without remaining outliers (Ref 14).

Detection of defects, then, being understood as a critical aspect of qualifying L-PBF components (Ref 15), would typically require some method(s) of nondestructive testing (NDT). Given the digital nature of the AM process, in situ sensing for the detection of processing flaws—a non-traditional application of NDT principles—has been the subject of much research in recent years (Ref 16-19), in an effort to accelerate the qualification process. In situ inspection and qualification is desirable for sustained adoption of AM, but is still in a developmental phase. More traditional NDT technologies like x-ray computed tomography (XCT) continue to be relied upon as "ground truth" verification of flaw populations in AM components (Ref 20).

The need to quantify the detection capabilities of nondestructive testing (NDT) methods has long been identified [cite AFRL POD handbook], and the same is true of XCT. There is a broad knowledge base around the impact that various XCT technique parameters have on the reconstructed volume (Ref 21), and methods have been developed for quantifying resolution and contrast discrimination (Ref 22). The capabilities of XCT and other NDT techniques are also being enhanced using artificial intelligence and machine learning-based ap-

This invited article is part of a special topical issue of the *Journal of Materials Engineering and Performance* on Advanced Materials Manufacturing. The issue was organized by Antonello Astarita, University of Naples Federico II; Glenn S. Daehn, The Ohio State University; Emily Kinser, ARPA-E; Govindarajan Muralidharan, Oak Ridge National Laboratory; John Shingledecker, Electric Power Research Institute, Le Zhou, Marquette University, and William Frazier, Pilgrim Consulting, LLC, and Editor, *JMEP*; on behalf of the ASM International Advanced Manufacturing Technical Committee.

Griffin Jones, Marissa Stecko, and **Jayme Keist**, The Pennsylvania State University Applied Research Laboratory, University Park; and **Veeraraghavan Sundar** and **Rachel Reed**, UES, A BlueHalo Company, Arlington. Contact e-mail: gtj109@arl.psu.edu.

Published online: 25 November 2024

proaches (Ref 23-26). The standardized measures of spatial resolution and contrast discrimination are helpful and needed, but do not purport to translate directly to detection of flaws of a given size, which is of critical importance for the use of AM parts in fatigue-critical applications. Therefore, methods of verifying the performance of XCT at flaw detection have been explored. Poudel et al. developed a scheme for classifying defects as lack of fusion, gas-entrapped porosity or keyhole porosity based on the morphology revealed in XCT data (Ref 27). Improving the fidelity of the reconstructed XCT data—-which would yield direct improvements to both the morphology resolution of large flaws and the contrast resolution of smaller flaws—through the use of a deep learning approach assisted by CAD models and x-ray–material interaction simulations has also been demonstrated (Ref 28). The effect of a fractional factorial experiment of XCT acquisition parameters on image quality has also been studied, along with the probability of detection of embedded flaws with those various XCT techniques (Ref 24).

Serial sectioning is another available method for validating XCT data and has been used successfully in the biological (Ref 29-31) and materials characterization (Ref 32) fields. One earlier study showed the inability of XCT to detect defects approximately 200 × 150 × 100 μm located 530 μm below the surface that were revealed by serial sectioning (Ref 33). Groeber et al. concluded from limited optical microscopy that an XCT scan with voxel size 23 μm was not able to detect flaws below 50 μm, and not able to well represent flaw morphology below 200 μm (Ref 34). Most closely related to the present work, Jolley et al. used destructive serial sectioning as a higher fidelity method against which to compare XCT, showing the limitations of XCT at revealing the size and morphology of flaws in a LBPF Ti-6Al-4V sample (Ref 35). Prior work by some of the current authors demonstrated a similar approach to using automated optical serial sectioning (AOSS) tools as a verification method for XCT (Ref 36). Whereas these past efforts have focused on intense study of defects present in a single sample, the current work investigates detectability of flaws in XCT on a broader scale, examining the defect populations as revealed by AOSS and XCT in multiple L-PBF samples.

2. Experimental Methods

2.1 Sample Fabrication and Fatigue Testing

Fabrication and fatigue testing details were originally reported in (Ref 37) and are summarized here. Samples were fabricated via laser powder bed fusion (L-PBF) on a 3D Systems ProX 320 using OEM-recommended parameters for 60 μm layers with Grade 23 Ti-6Al-4V virgin (Ref 38). Four (4) samples originating from different cluster locations of build C003 were selected at random and remained in the as-deposited (vice post-HIP) condition to increase the observable flaw population. Each sample was machined to a diameter of 12.70 mm and a height of 81.80 mm, leaving the sample identification number intact (Figure 1). As reported in (Ref 37), other samples from this build were fatigue tested at a maximum stress level of 827 MPa (120 ksi) and a stress ratio of R = + 0.1 by Element Materials Technology (Fairfield, OH).

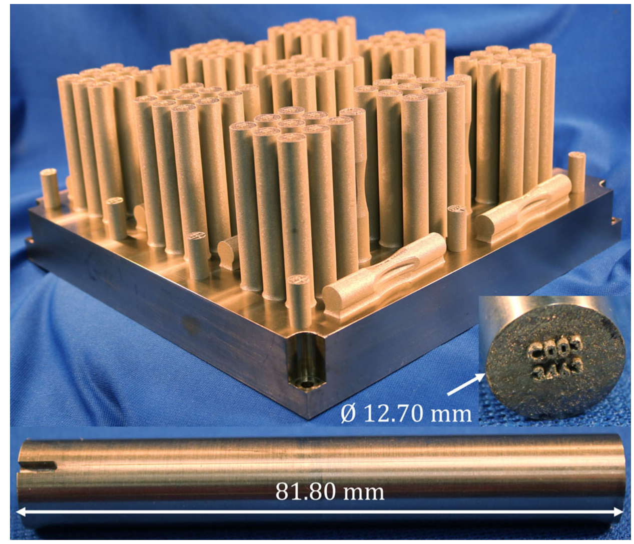

Fig. 1 Photographs of the L-PBF build plate with fatigue specimen clusters and of one of the samples selected for this work, machined to final dimensions with the specimen identification intact on its top face

2.2 X-ray Computed Tomography and Automated Optical Serial Sectioning

X-ray computed tomography was performed on the samples with two different commercial XCT systems: a Waygate Technologies v|tome|x L 300 and v|tome|x M 300, each using a 300 kV micro-focus x-ray source. Scans were acquired at a range of voxel sizes in order to develop an understanding of the relationship between voxel size and flaw detectability. The first voxel size, 43 μm, allowed for the entirety of each sample to be captured in one field of view of the XCT system digital detector, representative of how industry might minimize scan time and cost. Two of the samples—numbers 3463 and 3481—were selected for XCT interrogation at higher resolution voxel sizes, 12 μm and 25 μm. The 12 μm voxel size was chosen as the smallest possible which still allowed for sufficient power output from the x-ray source to penetrate the sample, and the 25 μm voxel size was chosen as approximately double the 12 μm.

Automated optical serial sectioning (AOSS) was performed on the samples using a UES Robo-Met.3D® system, which sequentially grinds and polishes away layers of material with micron level accuracy followed by optical microscope imaging. To prepare the samples, a portion of the machined cylinder containing the sample label was removed and mounted in epoxy along with three (3) titanium spheres to be used for image registration and material removal rate calculation ($\sim$5 μm/section). An optical microscope using a 5X objective captured a montage of stitched images of the entire polished surface, the montage having an XY resolution of $\approx$ 2 μm/pixel. A summary of the XCT and AOSS parameters for each of the samples is shown in Table 1.

2.3 Data Registration, Flaw Identification and Flaw Validation

To reduce misalignment errors and raw data size, AOSS images were cropped by a consistent X and Y distance relative to the centroids of the co-mounted spheres. Material removal

Table 1 Select parameters from XCT and AOSS data acquisition on the four (4) samples

Sample	3421	3439	3463	3481
Acquired XCT data				
43 μm	✔	✔	✔	✔
25 μm	…	…	✔	✔
12 μm	…	…	✔	✔
XCT parameters	Voltage (kV)	Amperage (μA)	Images	Filter
43 μm	260	160	800	0.5 mm Sn (source),
25 μm	260	95	2x 800	0.5 mm Cu (detector)
12 μm	200	70	3x 1500	0.5 mm Sn (source)
AOSS parameters				
Material removal (μm)	2100	2100	2000	1300
XY resolution (μm)	2.09	2.09	1.78	2.09

per slice was calculated by measuring the apparent sphere diameters in a given image relative to the true sphere diameters, with the average from the three spheres set as the raw Z resolution of the AOSS image stack. To ensure isometric resolution of the 3D AOSS image stack, a bi-cubic interpolation was performed on the voxel values to up-sample the data to match the native XY resolution shown in Table 1. The XCT and AOSS data sets were then registered to the same coordinate system using Volume Graphics VGStudio MAX® software as described in (Ref 36). This registration process involved first manually aligning the data sets as closely as possible and then using the "Best fit registration" tool in VGStudio MAX®.

It should be noted here that edge rounding of the fiducial spheres during the metallographic serial sectioning process could have contributed to error in calculation of the sphere centroids and measurement of the sphere diameters. One recent study using a similar AOSS process with Ti-6Al-4V fiducial spheres observed that although the most extreme effect of edge rounding to occur after restarts in the AOSS process, with instantaneous (difference of one slice) changes in diameter of typically 2.5-5.5% (Ref 39). Although no measurement of sphere edge rounding or compensation thereto was performed in this work, if a similar degree of edge rounding occurred during restarts to the AOSS process, this would result in—for an example slice from sample 3463—a 35-76 μm change in the Z-step calculation. For this sample, the largest calculated Z-step between AOSS slices was 7.56 μm, and so it would seem that the same degree of edge rounding due to restarts was not observed in this study, perhaps due to a difference in metallographic procedure. Due to the small Z-dimension of material that was sectioned, the full diameter of the spheres (9.52 mm) was not exposed in the AOSS slices, and so it is difficult to comment on the size of the error caused by sphere edge rounding during the steady-state regimes of the AOSS process. However, as the Z-step calculations relied on the *relative* slice-to-slice diameter change in the spheres, assuming that the degree of edge rounding was consistent from slice-to-slice, the calculations would not have been significantly impacted.

Flaw identification in the XCT and AOSS data sets made use of an in-house automated defect recognition (ADR) algorithm developed in MATLAB (Ref 40). A priori review of the data sets and iteration were used to finalize algorithm parameters, including the quantity and size of convolution kernels, the standard deviation threshold for flagging anomalies, and the minimum cluster size. Attributes for each flaw cluster were tabulated, and images of each flaw were reviewed manually, resulting in classification of each flaw as a true positive (real flaw) or false positive (not real flaw).

3. Results and Discussion

3.1 Microstructure and Fatigue Life

Figure 2 shows optical micrographs of as-deposited witness coupon material from the build plate. A lamellar structure of α' in prior β grains is evident, with the scale of β grains on the order of 100-200 μm, consistent with other observations (Ref 12). Microstructural analysis and fatigue results of the post-HIP fatigue tested specimens were provided in (Ref 37) and summarized here. After HIP, the microstructure was converted from martensitic α' to $\alpha + \beta$ with an average alpha lath width of 1.92 ± 0.21 μm and no apparent texturing of the prior β grains. As all of the specimens were tested at the same conditions, a traditional S-N curve was not developed, but rather a box-and-whisker plot in terms of $\log_{10}$ cycles to failure, with a mean of 5.83, median of 6.06 and variance of 0.29.

3.2 Detected Flaws in XCT and AOSS Data Sets

An increase in flaw detectability with refinement of the XCT voxel size was readily observed. Figure 3 illustrates this with a comparison of registered slices of XCT and AOSS data for sample 3463, and Figure 4 shows the corresponding ADR output. The two largest flaws are clearly visible in the slice in Figure 3 in all XCT data, with additional flaws not detectable until the XCT voxel size reduces to 12 μm. Three of the four additionally resolved flaws have a corresponding match in the AOSS data, with higher magnification images of a select flaw showing similar morphology and size. The fourth flaw that was not matched (an open circle in Figure 3d) is due to registration error—the flaw is present at a different z-height of the AOSS data. A two orders of magnitude greater quantity of flaws were detected in the AOSS data (Figure 4).

Histograms comparing the validated flaw populations in the AOSS (red) and XCT (blue) data as a function of the volume equivalent spherical diameter (ESD)—selected due to the approximately spherical morphology of many stochastic flaws—are shown in Figure 5. The solid black line represents the percentage of AOSS flaws detected in the XCT data sets for

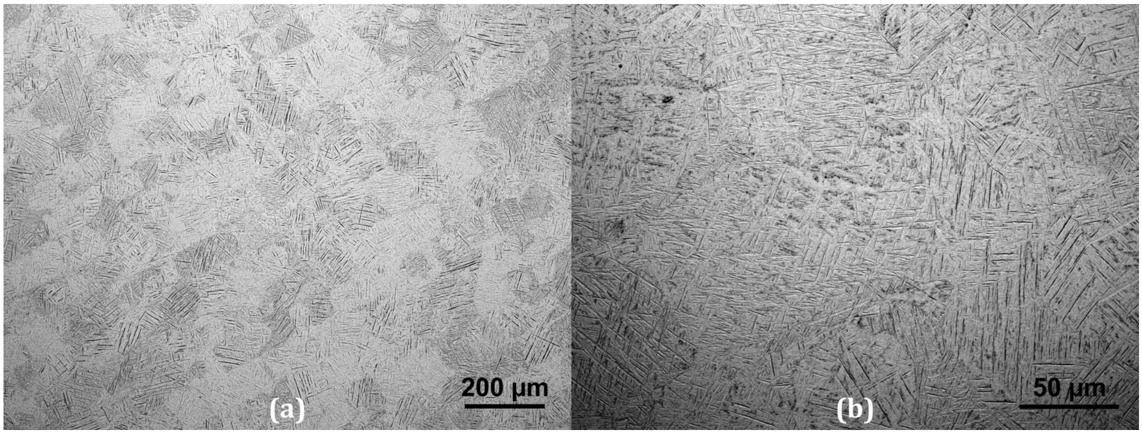

Fig. 2 Optical micrographs of as-deposited witness material from the L-PBF build at (a) lower and (b) higher magnification, both revealing an α' microstructure in prior β grains, with no particular texturing of the β grains

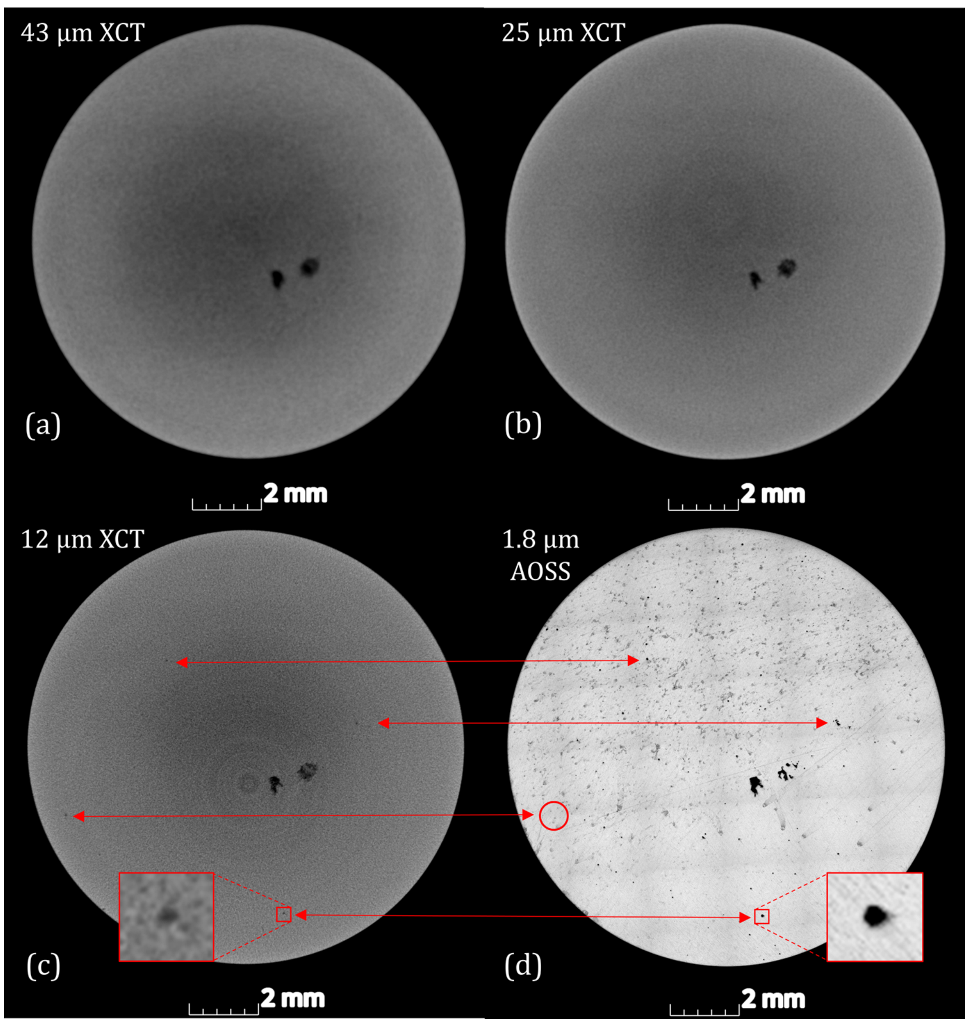

Fig. 3 Comparison of a registered slice of XCT and AOSS data from sample 3463. (a) 43 μm voxel XCT data; (b) 25 μm voxel XCT data and (c) 12 μm voxel XCT data with arrows indicating the corresponding flaw in (d) 1.8 μm voxel AOSS data

a given histogram bin, and the dashed black line is a sigmoidal fit of the relationship between detection percentage and flaw size. The limited quantity of flaws above 200 μm and the mischaracterization of flaw size in some cases by XCT (discussed below) prevented a smooth sigmoidal fit.

The 43 μm XCT data show no detection of flaws below an ESD of 150 μm. For samples 3421 and 3439, this included 0 detected flaws compared to over 2000 in the corresponding AOSS data, all at an ESD of $\leq$ 119 μm. This would support the radiographic principle that features < 3 voxels across

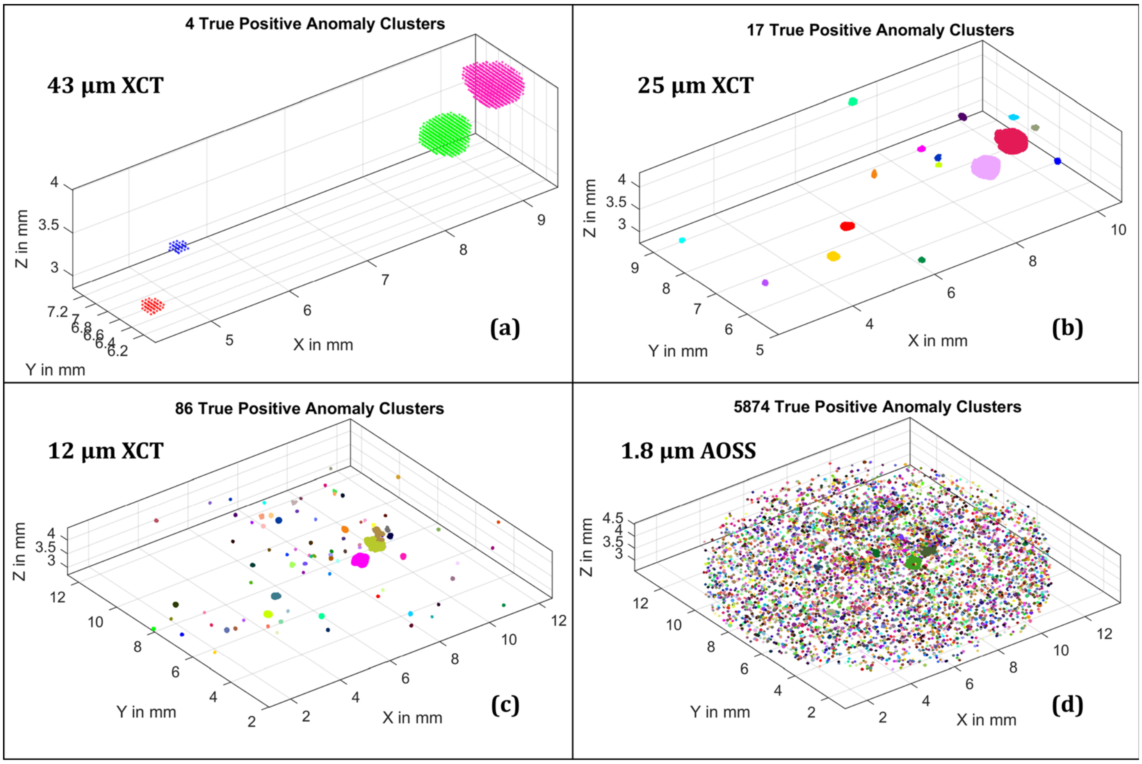

Fig. 4 Validated flaws from ADR output for sample 3463, comparing the (a) 43 μm, (b) 25 μm and (c) 12 μm voxel size XCT data with the (d) 1.8 μm voxel size AOSS data

cannot be reliably detected by XCT. A total of four flaws were detected in the 43 μm XCT data for sample 3463; two of 150-200 μm and two 450-550 μm ESD. The smaller two flaws matched the histogram bin size for four corresponding flaws in the AOSS data, whereas the 450-550 μm flaws did not size match with flaws in the AOSS data. Slice imagery revealed that the 450-550 μm diameter XCT flaws corresponded to two 300-400 μm AOSS flaws; the histogram reports a 0% XCT detection rate for this bin size. Thus, XCT may artificially inflate flaw sizes, presumably due to coarser resolution and the partial volume effect. For sample 3481, one flaw of ESD 171 μm was detected at 43 μm, compared to over 1900 flaws in the AOSS data.

Although the histogram for 43 μm XCT data portrays the 90% detection rate as being first achieved at an ESD of 250-300 μm, this bin is empty for the AOSS data, so no detection rate data are available here. In light of the mischaracterization of flaw sizes by the XCT data discussed above, the XCT histogram detection rate would first reach 90% for an AOSS flaw diameter of 300 μm, or approximately *7 times the voxel size*. As there is only (1) AOSS flaw at this size, however, it is uncertain if this sevenfold relationship would hold true for a larger population of flaws. A 20% histogram detection rate for 100-150 μm ESD flaws was observed in the 25 μm XCT data (compared to 0% for 43 μm XCT), and a 90% detection rate was first achieved for a flaw size of just over 200 μm, or about *8 times the voxel size*. For the 25 μm XCT data—as with the 43 μm data—the small quantity of flaws at this size scale makes it difficult to predict the applicability of this relationship across larger flaw populations.

For the 12 μm voxel XCT data, just under 30 flaws in the 1-50 μm ESD range were detected, the smallest of which was 44 μm in diameter, although the histogram detection rate in this 1-50 μm diameter size range was still small at 0.3%. Over 130 flaws 50-100 μm in ESD were found in the XCT data for a detection rate of 6%, and an 80% detection rate was achieved in the range of 150-200 μm. However, in the 200-250 μm size range, more flaws were detected in the XCT data than in the AOSS data (detection rate $>$ 100%). One of the corresponding AOSS flaws was also 200-250 μm, but the others were found in the 100-150 μm and 150-200 μm ESD bins of the histogram. Therefore, a 90% histogram detection rate for the 12 μm XCT data would first be achieved for a true flaw ESD of 150-200 μm, which is *12-17 times the voxel size*. This is a degradation in flaw detectability as a function of voxel size compared to the 43 μm (7 times) and 25 μm (8 times) XCT data, possibly due to a decrease in contrast resolution from the limited x-ray signal used to acquire the 12 μm XCT scans.

This approach to assessing the detection limits of XCT is dependent upon accurate sizing of flaws by the ADR algorithm. Although direct accuracy statements about the ADR flaw sizing cannot be made, a corroboration of some of the flaw sizes was performed using the porosity analysis module in VGStudio MAX® software. The VGDefX algorithm, using deviation auto-threshold mode, deviation factor of 0.00, medium noise reduction, general probability criterion and a probability threshold of 0.90, was applied to the 43 μm and 25 μm XCT data sets for sample 3463, resulting in 15 flaws matched (4 of which were present in both data sets) with those identified by the MATLAB ADR algorithm. Flaw ESD's ranged from 104 to 517 μm for ADR and 108 to 497 μm for VG, matched flaws differing by 2.3-32.9%, with eight (8) of the VG flaws being smaller than their MATLAB ADR match, and the other seven (7) being larger.

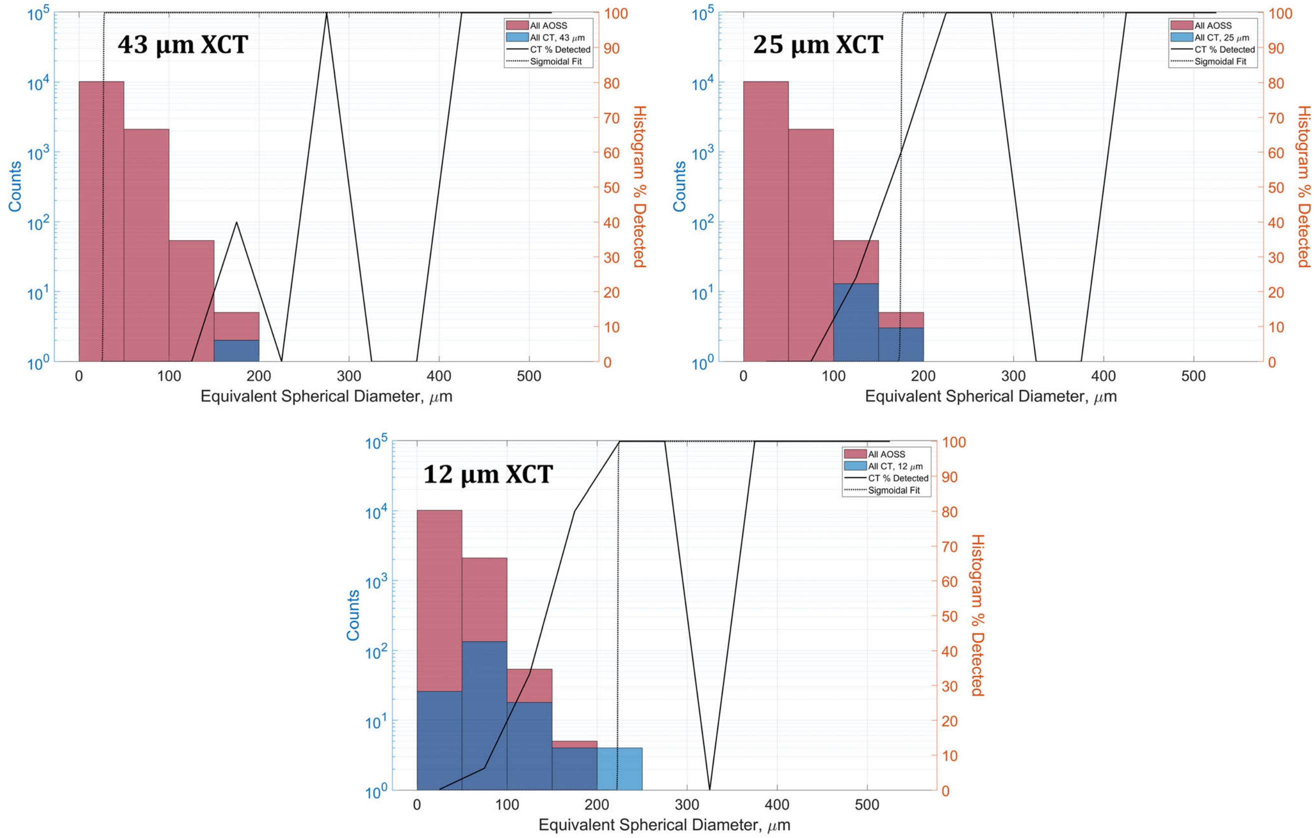

Fig. 5 Histograms comparing the validated flaw populations between the AOSS (red) and XCT (blue) data sets for all samples, separated by XCT voxel size. The thick black line represents the percentage of AOSS flaws (ground truth) detected in the XCT data sets, and the dashed black line is a sigmoidal fit of the relationship between detection percentage and flaw size, expressed as spherical equivalent diameter (μm) (Color figure online)

Magnitude of the ESD differences formed into two clusters, one for flaws 100-200 μm and one for flaws 450-525 μm, with an average difference of 20.7 μm for the smaller 11 flaws and 46.8 μm for the larger four. These larger flaws were all sized as smaller by VG compared to the ADR, the largest ESD difference being 76.8 μm, for a 479 μm ADR flaw sized at 402 μm by VG. This finding supports the observation of inflation of XCT flaw size for larger flaws as discussed above. Thus, for flaws $\leq$ 200 μm, the true histogram bin is expected to be less than $\pm$ 0.5 bins of that reported, and for flaws $>$ 400 μm, the true histogram bin is expected to be within + 0/-2 bins of that reported. Although these findings could potentially improve the voxelized detection rates reported above, additional flaw populations should be studied before such conclusions are drawn.

4. Conclusion

The detectability of features in radiographic data is not simply a factor of spatial resolution, but rather a complicated function of many variables affecting both the contrast resolution and spatial resolution of the imagery. However, the voxel size is inarguably at the foundation of the spatial resolution of a given XCT data set, and therefore, the present results are discussed in relation to that acquisition parameter in order to develop a relationship between voxel size and defect detectability. This work supports the rule that the smallest flaw that can be resolved in a given XCT data set is 3 times the voxel size; however, the detection rate at this size is low, less than 1% for the flaw populations studied here. The historically relevant 90% detection rate was achieved between a broad range of *7-17 times the voxel size* and varied with the voxel size of the acquired XCT scan.

Flaw detectability rates for the 43 μm and 25 μm XCT data are difficult to broadly apply due to the low ($<$ 100) quantity of flaws of ESD $\leq$ 150 μm present in the L-PBF samples—the size where those XCT data sets began to resolve flaws. Future work should target samples with a statistically significant population of flaws $\geq$ 6 times the voxel size of the XCT data in order to substantiate detection rates calculated here. Establishment of critical flaw sizes for L-PBF components could assist in quantifying the relevance of higher resolution in both XCT and the AOSS. Accordingly, poorer contrast discrimination in the 12 μm XCT scan is thought to be responsible for its degraded detection rate per voxel size relative to the other XCT scans. Relationship between established measurements of XCT image data quality—such as the modulation transfer function (MTF), contrast discrimination function (CDF) (Ref 22) and/or contrast-detail-dose diagram (CDD) (Ref 21)—and the voxel size detection rate dependency should be studied to yield practical guidance for the application of XCT.

Acknowledgment

This work was performed through the National Aeronautics and Space Administration SBIR Contract 80NSSC21C0586, titled, "Probability of Detection and Validation for Computed Tomography Processes for Additive Manufacturing." The authors would like to thank Madison Reents and the Robo-Met team at UES; Matthew Pantano for data processing support; Jacob Morgan and Jan Petrich for refinement of the ADR tools and Timothy Stecko for acquisition of XCT data.

References

1. T. Ngo, A. Kashani, G. Imbalzano, K. Nguyen, and D. Hui, Additive Manufacturing (3D Printing): A Review of Materials, Methods, Applications and Challenges, *Compos. PART B-Eng.*, 2018, **143**, p 172–196
2. W. Frazier, Metal Additive Manufacturing: A Review, *J. Mater. Eng. Perform.*, 2014, **23**(6), p 1917–1928
3. D. Gu, W. Meiners, K. Wissenbach, and R. Poprawe, Laser Additive Manufacturing of Metallic Components: Materials, Processes and Mechanisms, *Int. Mater. Rev.*, 2012, **57**(3), p 133–164
4. X. Peng, S. Wu, W. Qian, J. Bao, Y. Hu, Z. Zhan, G. Guo, and P.J. Withers, The Potency of Defects on Fatigue of Additively Manufactured Metals, *Int. J. Mech. Sci.*, 2022, **221**, 107185
5. A. Li, S. Baig, J. Liu, S. Shao, and N. Shamsaei, Defect Criticality Analysis on Fatigue Life of L-PBF 17–4 PH Stainless Steel via Machine Learning, *Int. J. Fatigue*, 2022, **163**, 107018
6. T. DebRoy, H. Wei, J. Zuback, T. Mukherjee, J. Elmer, J. Milewski, A. Beese, A. Wilson-Heid, A. De, and W. Zhang, Additive Manufacturing of Metallic Components - Process, Structure and Properties, *Prog. Mater. Sci.*, 2018, **92**, p 112–224
7. Y.N. Hu, S.C. Wu, P.J. Withers, J. Zhang, H.Y.X. Bao, Y.N. Fu, and G.Z. Kang, The Effect of Manufacturing Defects on the Fatigue Life of Selective Laser Melted Ti-6Al-4V Structures, *Mater. Des.*, 2020, **192**, 108708
8. S. Wu, P. Withers, S. Beretta, and G. Kang, Tomography traces the growing cracks and defects, *Eng. Fract. Mech.*, 2023, **292**, p 109628
9. W. Qian, S. Wu, L. Lei, Q. Hu, and C. Liu, Time Lapse in Situ X-Ray Imaging of Failure in Structural Materials under Cyclic Loads and Extreme Environments, *J. Mater. Sci. Technol.*, 2024, **175**, p 80–103
10. T. Mower and M. Long, Mechanical Behavior of Additive Manufactured, Powder-Bed Laser-Fused Materials, *Mater. Sci. Eng. -Struct. Mater. Prop. Microstruct. Process.*, 2016, **651**, p 198–213
11. J. Günther, D. Krewerth, T. Lippmann, S. Leuders, T. Tröster, A. Weidner, H. Biermann, and T. Niendorf, Fatigue Life of Additively Manufactured Ti-6Al-4V in the Very High Cycle Fatigue Regime, *Int. J. Fatigue*, 2017, **94**, p 236–245
12. H. Masuo, Y. Tanaka, S. Morokoshi, H. Yagura, T. Uchida, Y. Yamamoto, and Y. Murakami, Influence of Defects, Surface Roughness and HIP on the Fatigue Strength of Ti-6Al-4V Manufactured by Additive Manufacturing, *Int. J. Fatigue*, 2018, **117**, p 163–179
13. R. Molaei, A. Fatemi, and N. Phan, Significance of Hot Isostatic Pressing (HIP) on Multiaxial Deformation and Fatigue Behaviors of Additive Manufactured Ti-6A1-4V Including Build Orientation and Surface Roughness Effects, *Int. J. Fatigue*, 2018, **117**, p 352–370
14. T. Merdes, E.W. Reutzel, W.F. Mitchell, G. Welsh, A. Lass, J. Waterman, K. Cobb, B. Briggs, and E. Kline, "Additively Manufactured MV-22B Osprey Flight Critical Components: Production Data for Witness Coupons and Test Specimens," The Pennsylvania State University Applied Research Laboratory, 2020
15. J.W. Pegues, S. Shao, N. Shamsaei, N. Sanaei, A. Fatemi, D.H. Warner, P. Li, and N. Phan, Fatigue of Additive Manufactured Ti-6Al-4V, Part I: The Effects of Powder Feedstock, Manufacturing, and Post-Process Conditions on the Resulting Microstructure and Defects, *Int. J. Fatigue*, 2020, **132**, 105358
16. L. Kong, X. Peng, Y. Chen, P. Wang, and M. Xu, Multi-Sensor Measurement and Data Fusion Technology for Manufacturing Process Monitoring: A Literature Review, *Int. J. Extreme Manuf.*, 2020, **2**(2), p 022001
17. S.K. Everton, M. Hirsch, P. Stravroulakis, R.K. Leach, and A.T. Clare, Review of In-Situ Process Monitoring and in-Situ Metrology for Metal Additive Manufacturing, *Mater. Des.*, 2016, **95**, p 431–445
18. Y. AbouelNour and N. Gupta, In-Situ Monitoring of Sub-Surface and Internal Defects in Additive Manufacturing: A Review, *Mater. Des.*, 2022, **222**, 111063
19. R. McCann, M.A. Obeidi, C. Hughes, É. McCarthy, D.S. Egan, R.K. Vijayaraghavan, A.M. Joshi, V.A. Garzon, D.P. Dowling, P.J. McNally, and D. Brabazon, In-Situ Sensing, Process Monitoring and Machine Control in Laser Powder Bed Fusion: A Review, *Add. Manuf.*, 2021, **1**(45), p 102058
20. E. Cakmak, P. Bingham, R.W. Cunningham, A.D. Rollett, X. Xiao, and R.R. Dehoff, Non-Destructive Characterization of Additively Manufactured Components with x-Ray Computed Tomography for Part Qualification: A Study with Laboratory and Synchrotron x-Rays, *Mater Charact*, 2021, **1**(173), p 110894
21. ASTM International, "E1441-19 Standard Guide for Computed Tomography (CT)," ASTM International, West Conshohocken PA, 2019
22. ASTM International, "E1695-20e1 Standard Test Method for Measurement of Computed Tomography (CT) System Performance," ASTM International, West Conshohocken PA, 2020
23. Y. Fu, A.R.J. Downey, L. Yuan, T. Zhang, A. Pratt, and Y. Balogun, Machine Learning Algorithms for Defect Detection in Metal Laser-Based Additive Manufacturing: A Review, *J. Manuf. Process.*, 2022, **75**, p 693–710
24. F.H. Kim, A.L. Pintar, S.P. Moylan, and E.J. Garboczi, The Influence of X-Ray Computed Tomography Acquisition Parameters on Image Quality and Probability of Detection of Additive Manufacturing Defects, *J. Manuf. Sci. Eng.*, 2019, **141**(11), p 111002
25. C. Wang, X.P. Tan, S.B. Tor, and C.S. Lim, Machine Learning in Additive Manufacturing: State-of-the-Art and Perspectives, *Addit. Manuf.*, 2020, **36**, 101538
26. E. Vaghefi, S. Hosseini, M. Azimi, A. Shmatok, R. Zhao, B. Prorok, and E. Mirkoohi, Volumetric Defect Classification in Nano-Resolution X-Ray Computed Tomography Images of Laser Powder Bed Fusion via Deep Learning, *J. Manuf. Process.*, 2024, **121**, p 499–511
27. A. Poudel, M.S. Yasin, J. Ye, J. Liu, A. Vinel, S. Shao, and N. Shamsaei, Feature-Based Volumetric Defect Classification in Metal Additive Manufacturing, *Nat. Commun.*, 2022, **13**(1), p 6369
28. A. Ziabari, S.V. Venkatakrishnan, Z. Snow, A. Lisovich, M. Sprayberry, P. Brackman, C. Frederick, P. Bhattad, S. Graham, P. Bingham, and R. Dehoff, Enabling Rapid X-Ray CT Characterisation for Additive Manufacturing Using CAD Models and Deep Learning-Based Reconstruction, *npj Comput. Mater.*, 2023, **9**(1), p 91
29. J. Streicher, T. Weninger, and G. Muller, External Marker-Based Automatic Congruencing: A New Method of 3D Reconstruction from Serial Sections, *Anat. Rec.*, 1997, **248**(4), p 583–602
30. M. Groseclose, P. Massion, P. Chaurand, and R. Caprioli, High-Throughput Proteomic Analysis of Formalin-Fixed Paraffin-Embedded Tissue Microarrays Using MALDI Imaging Mass Spectrometry, *Proteomics*, 2008, **8**(18), p 3715–3724
31. J.E. Iglesias, R. Insausti, G. Lerma-Usabiaga, M. Bocchetta, K. Van Leemput, D.N. Greve, A. Van der Kouwe, B. Fischl, C. Caballero-Gaudes, and P.M. Paz-Alonso, Alzheimer's Disease Neuroimaging Initiative. A Probabilistic Atlas of the Human Thalamic Nuclei Combining Ex Vivo MRI and Histology, *Neuroimage*, 2018, **1**(183), p 314–326
32. T. Stan, Z. Thompson, and P. Voorhees, Optimizing Convolutional Neural Networks to Perform Semantic Segmentation on Large Materials Imaging Datasets: X-Ray Tomography and Serial Sectioning, *Mater Charact*, 2020, **160**, p 110119
33. S. Everton, P. Dickens, C. Tuck, B. Dutton, D. Wimpenny, and M.& M.S. Minerals, "The Use of Laser Ultrasound to Detect Defects in Laser Melted Parts," 2017, p 105–116
34. M. Groeber, E. Schwalbach, S. Donegan, K. Chaput, T. Butler, J. Miller, and IOP, "Application of Characterization, Modelling, and Analytics towards Understanding Process-Structure Linkages in Metallic 3D Printing," 2017
35. B.R. Jolley, M.D. Uchic, D. Sparkman, M. Chapman, and E.J. Schwalbach, Application of Serial Sectioning to Evaluate the Performance of X-Ray Computed Tomography for Quantitative Porosity Measurements in Additively Manufactured Metals, *JOM*, 2021, **73**(11), p 3230–3239

36. Z. Snow, J. Keist, G. Jones, R. Reed, E. Reutzel, and V. Sundar, Flaw Identification in Additively Manufactured Parts Using X-Ray Computed Tomography and Destructive Serial Sectioning, *J. Mater. Eng. Perform.*, 2021, **30**(7), p 4965–4965
37. Z. Snow, C. Cummings, E.W. Reutzel, A. Nassar, K. Abbot, P. Guerrier, S. Kelly, S. McKown, J. Blecher, and R. Overdorff, Analysis of Factors Affecting Fatigue Performance of HIP'd Laser-Based Powder Bed Fusion Ti–6Al–4V Coupons, *Mater. Sci. Eng. A*, 2023, **864**, 144575
38. ASTM International, "F3001-14(2021) Standard Specification for Additive Manufacturing Titanium-6 Aluminum-4 Vanadium ELI (Extra Low Interstitial) with Powder Bed Fusion," ASTM International, West Conshohocken PA, 2021
39. B.R. Jolley, D.M. Sparkman, M.G. Chapman, E.J. Schwalbach, and M.D. Uchic, Correlative X-Ray Computed Tomography and Optical Microscopy Serial Sectioning Data of Additive Manufactured Ti-6Al-4V, *Integrating Mater. Manuf. Innov.*, 2024, **13**(3), p 746–757
40. J. Petrich and E. Reutzel, Automated Defect Recognition for Additive Manufactured Parts Using Machine Perception and Visual Saliency, *3D Print Add. Manuf.*, 2023, **10**(3), p 406–419